Supplement of Atmos. Chem. Phys., 19, 13189–13208, 2019
https://doi.org/10.5194/acp-19-13189-2019-supplement

Supplement of

Composition and origin of $PM_{2.5}$ aerosol particles in the upper Rhine valley in summer

Xiaoli Shen et al.

Correspondence to: Harald Saathoff (harald.saathoff@kit.edu)

In order to study the nature and origin of aerosols at a rural site in the upper Rhine valley, we conducted a stationary measurement campaign (TRAM01) in summer 2016, and applied a transport model COSMO-ART to help source apportionment and to achieve a better understanding of the impact of complex transport pattern on the field observations. In the main manuscript, we have mainly discussed two selected episodes, one is rich in sodium chloride and another is rich in organics. Here is the supporting information, including figures, as well as some detailed descriptions.

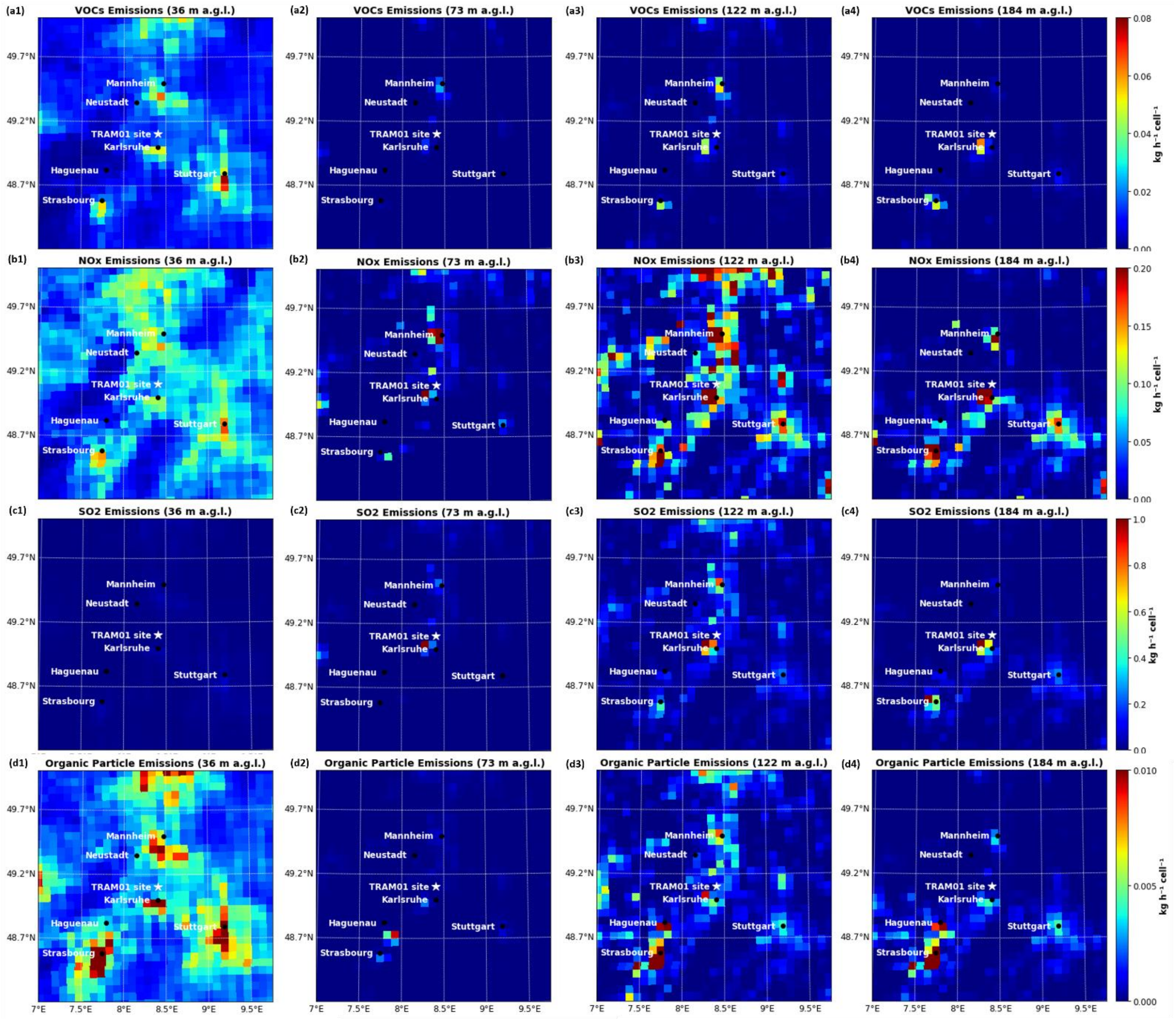

Figure S1: Emission maps of VOCs (a1 to a4), NOx (b1 to b4), SO_2 (c1 to c4), and primary organic particles (d1 to d4) at different altitudes, i.e., 36, 74, 122, and 184 m (from left to right) above ground level (a.g.l.).

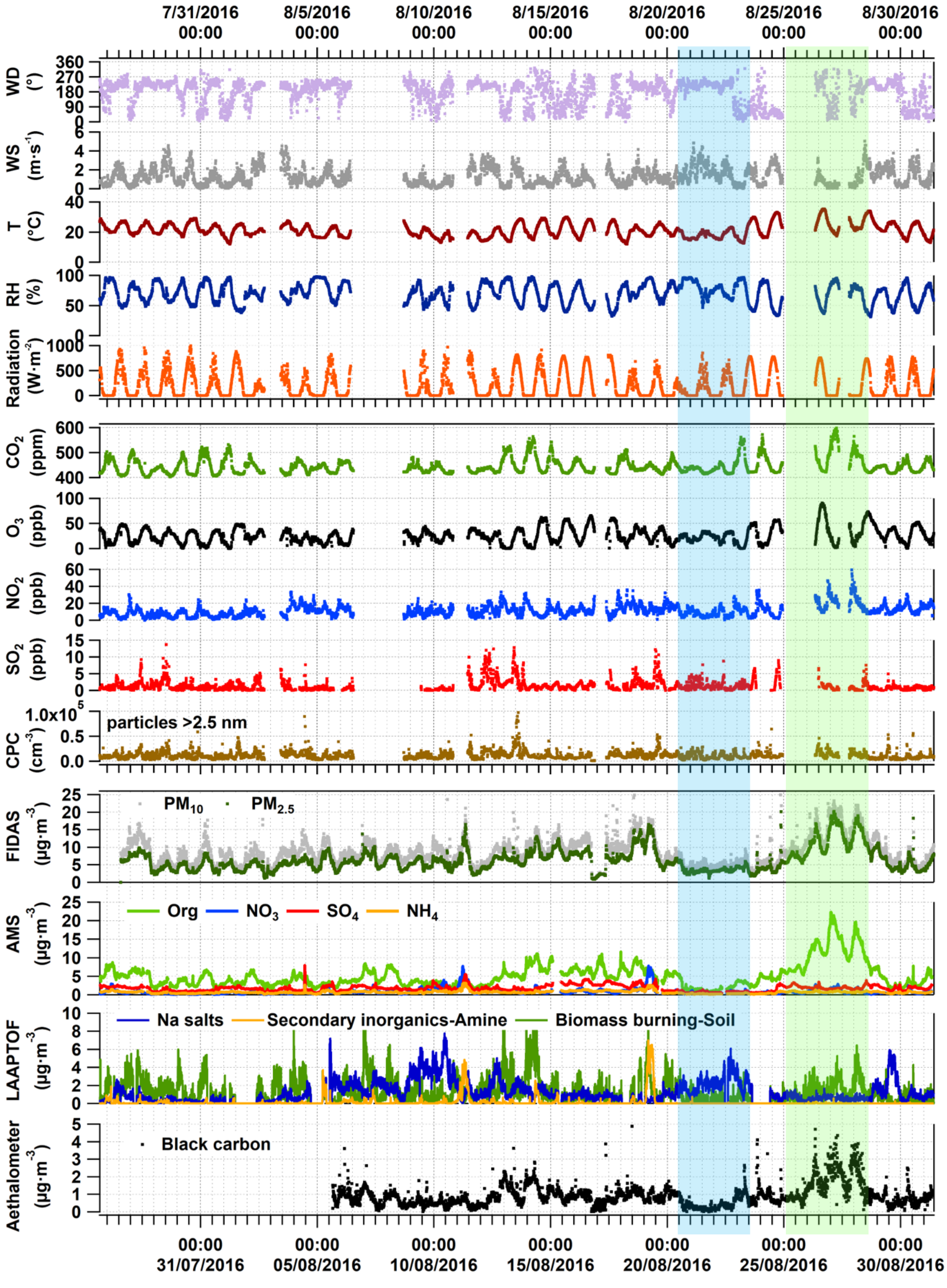

Figure S2: Overview of the whole measurement campaign including meteorology parameters, trace gases, and aerosol particle mass and composition. The first (blue) and second (green) shaded areas mark the sodium chloride rich and the organic rich episodes, respectively.

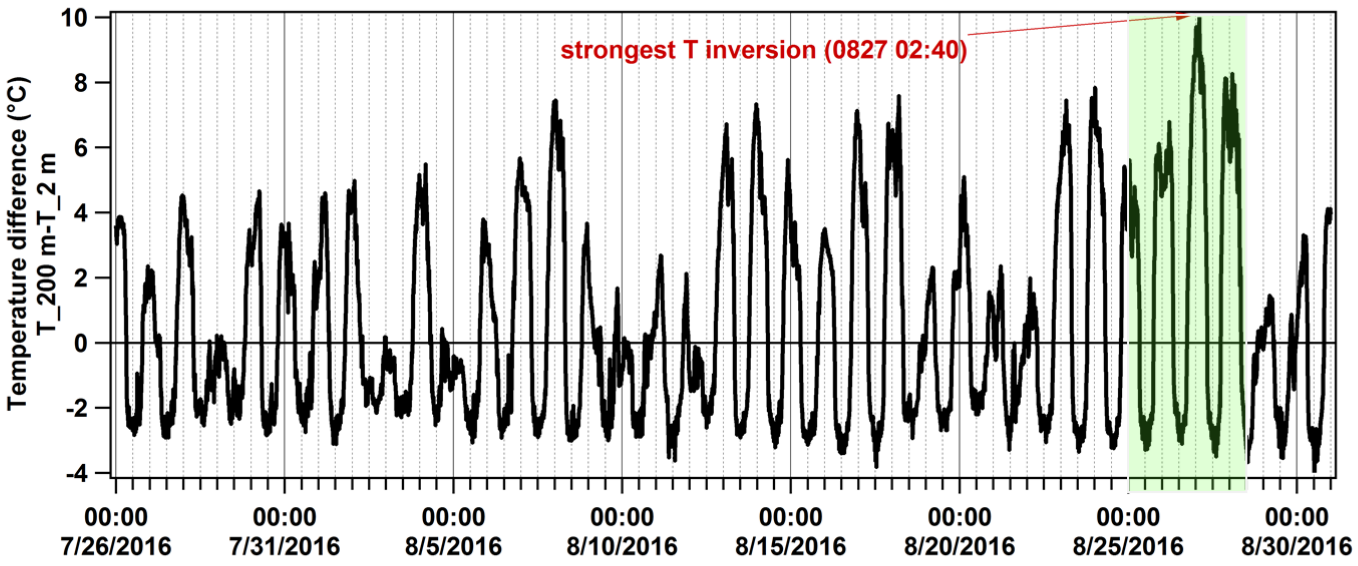

Figure S3: Time series of temperature difference between 200 m and 2 m above ground level (a.g.l.), measured at the KIT-tower. The bigger difference denotes the stronger temperature inversion. Temperature inversions are stronger during the organics rich episode marked with a shaded background. The strongest temperature inversion was measured at 02:40 on August 27.

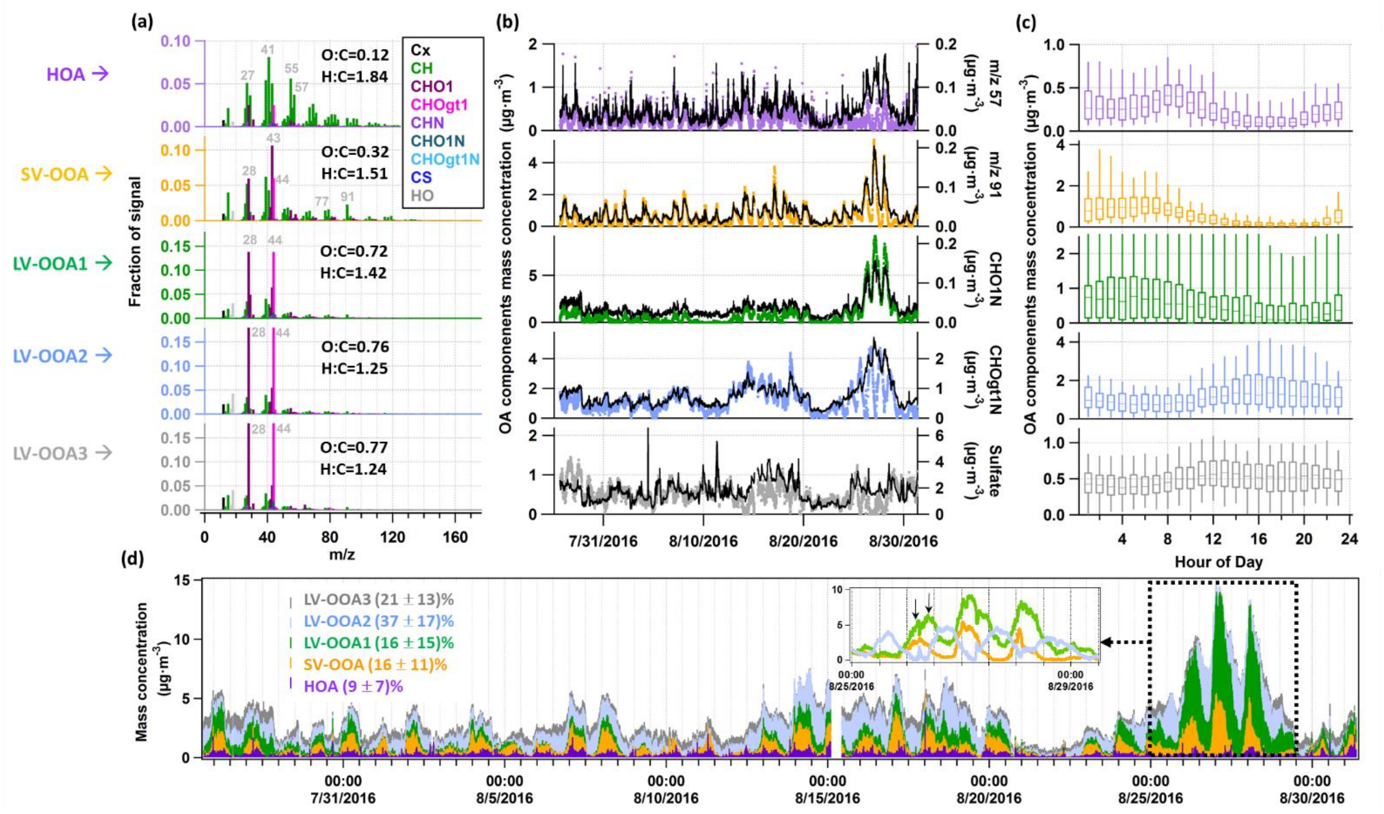

Figure S4: Five-factor-PMF solution with FPEAK=0 for organic compounds measured by AMS during the whole measurement time. (a) Mass spectra of the five components, i.e., HOA, SV-OOA, LV-OOA1, LV-OOA2, and LV-OOA3. Peaks are coloured with respect to different ion families. (b) Time series of the five components mass concentrations (left Y-axis) and their tracers or related ion family (right Y-axis). (c) Diurnal patterns of the five components. (d) Time series of the stacked components with the same data as panel (b), but the contribution of the five components can be visualized clearly. The percentages are their contributions to OA. The insert shows time series of SV-OOA, LV-OOA1 and LV-OOA2 during organic rich episode, and the two back arrows point out night-time and day time sub-peaks of the first LV-OOA1 peak. Note that the total OA value showed here is lower than the input OA for the PMF analysis. This is because the components identification might be interfered by extraneous variability, arising from some causes such as instrumental issues. Such extraneous variability will lead to disproportionate effects on the fitting outcome. Therefore, we need to downweight the corresponding variables in a proper way or even remove them, resulting the lower output total OA value reconstructed by the components.

The criteria for choosing factor number are given in section 2.2 of main manuscript. As shown in the Fig. S4 (a) HOA, SV-OOA, and LV-OOA have distinguishable spectra. For three LV-OOA, in spite of some similarity, distinguishable features can still be found, according to their time series (b) and diurnal patterns (c). In particular for the organic rich episode, LV-OOA1 and LV-OOA2 show anti-correlation, the LV-OOA3 signal is much weaker than the other two LV-OOA. Therefore, a five-factor solution was chosen rather than four or three-factor solution.

HOA is associated with POA, e.g., from urban emissions. In this study, the HOA (high H:C = 1.84 and low O:C = 0.12, herein) has a similar trend as m/z 57 (major contribution from C_4H_9) and NO_2 (not shown), with Pearson's correlation coefficients $\gamma = 0.5$ and 0.4, respectively. SV-OOA (O:C = 0.32) shows a very strong correlation with m/z 91 (mainly from C_7H_7) ($\gamma = 0.9$) and CH family ($\gamma = 0.8$). Three LV-OOA have prominent marker peaks at m/z 28 and 44, and all have high O:C ratio (> 0.7), which indicates highly oxidized or aged OA. LV-OOA1 shows strong correlations ($\gamma = 0.8$ to 1) with CH, CHO1, CHOgt1, CHN, CHO1N, and CHOgt1N. LV-OOA2 shows good correlations with CHOgt1N ($\gamma = 0.6$). LV-OOA3 shows no good correlation with any ion families, but a similar trend as sulfate ($\gamma = 0.5$).

Similar elemental ratios for HOA, SV-OOA, and LV-OOA and their relationships with tracers such as HOA with NOx and LV-OOA with secondary inorganics, have also been reported in previous AMS-PMF studies. Readers may refer to a review paper by Zhang et al. (2011).

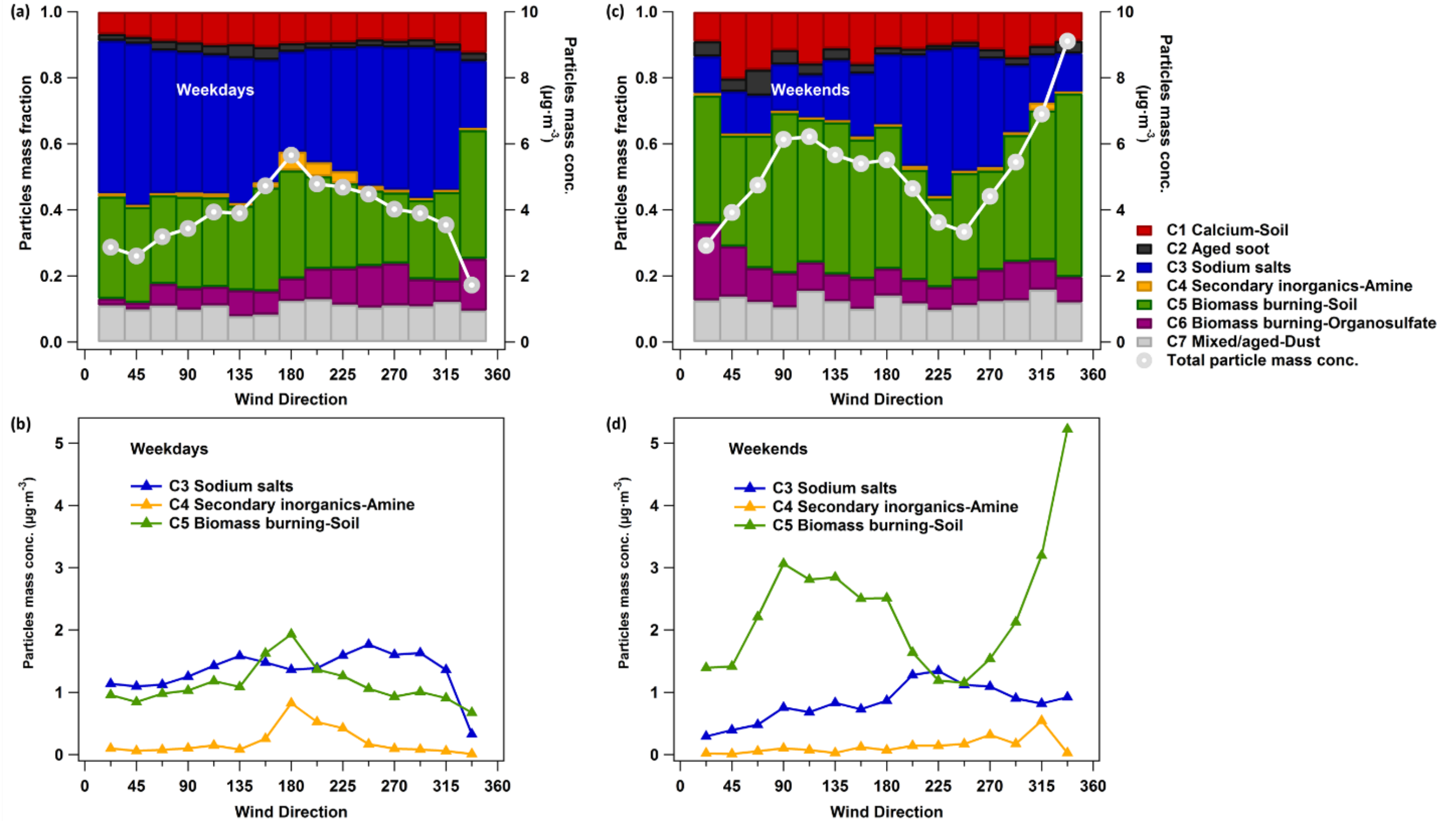

Figure S5: Comparison of particle classes measured by LAAPTOF as a function of wind direction for weekdays (left) and weekends (right). The data is averaged over the entire campaign. The data comprises 4842 time points of 10 min averaged data, including 3702 for weekdays and 1140 for weekends, including Saturday and Sunday. The total particle mass concentration for each wind direction is on average 3.8 (± 2.3, one σ) µg m^{-3} and 5.2 (± 3.0) µg m^{-3} during weekdays and the weekends, respectively. For the dominating particle classes the average mass concentrations are 1.3 (± 1.2) µg m^{-3} and 0.8 (± 0.5) µg m^{-3} for class 3, 0.2 (± 0.5) µg m^{-3} and 0.1 (± 0.2) µg m^{-3} for class 4, 1.1 (± 1.0) µg m^{-3} and 2.3 (± 1.7) µg m^{-3} for class 5, for weekdays and weekends respectively.

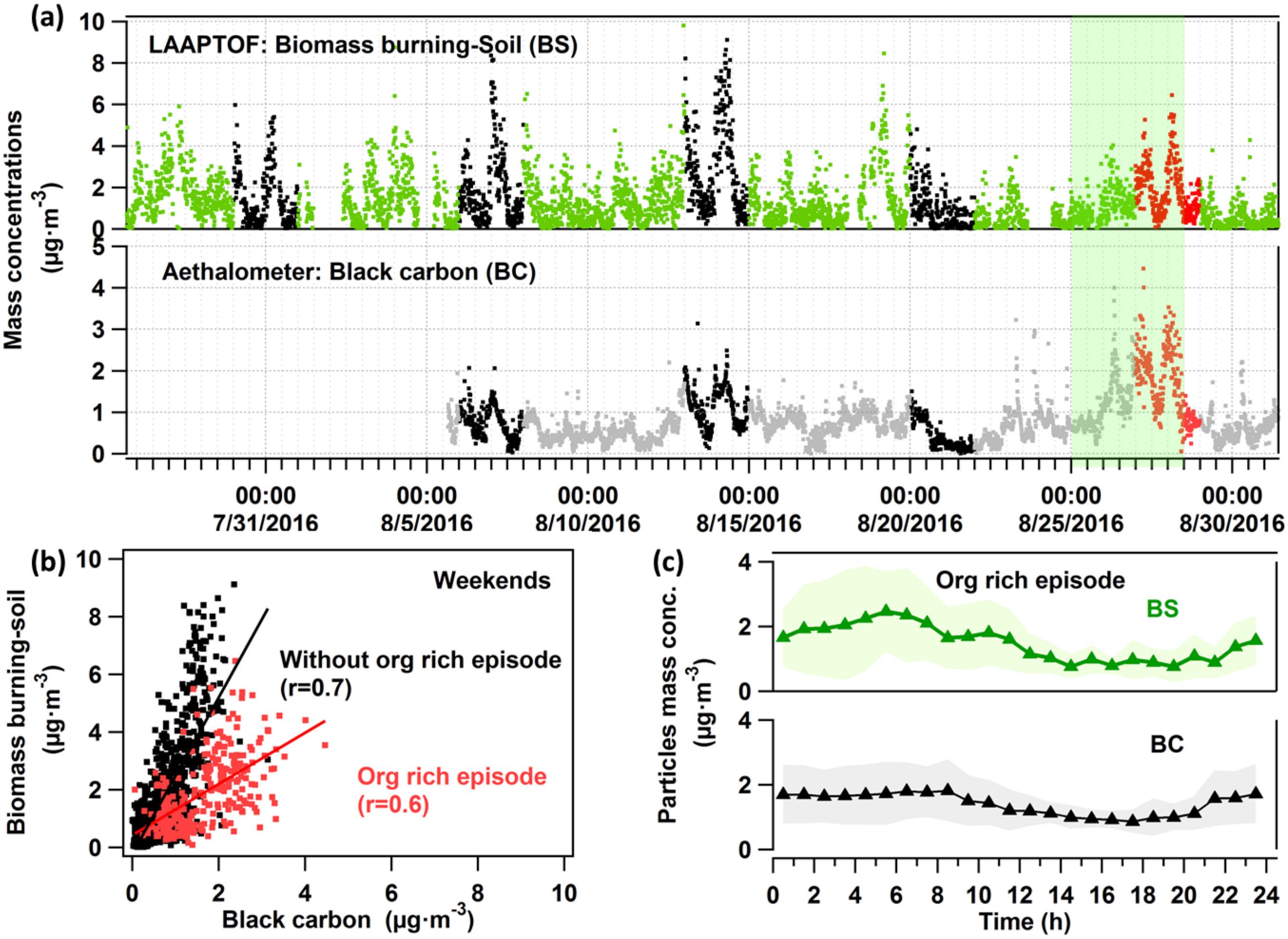

Figure S6: (a) Time series of aged-biomass-burning and soil-dust like particles and black carbon (black and red dots are weekend data); red dots are in organics rich episode. The shaded area marks the organics rich episode. (b) Comparison of mass concentration between biomass burning-soil and black carbon measured during the weekends. Black and red dots are the data without and with organic rich episode, respectively. (c) Diurnal pattern of particle mass concentration of biomass burning-soil (BS) and black carbon (BC) during organics rich episode, respectively.

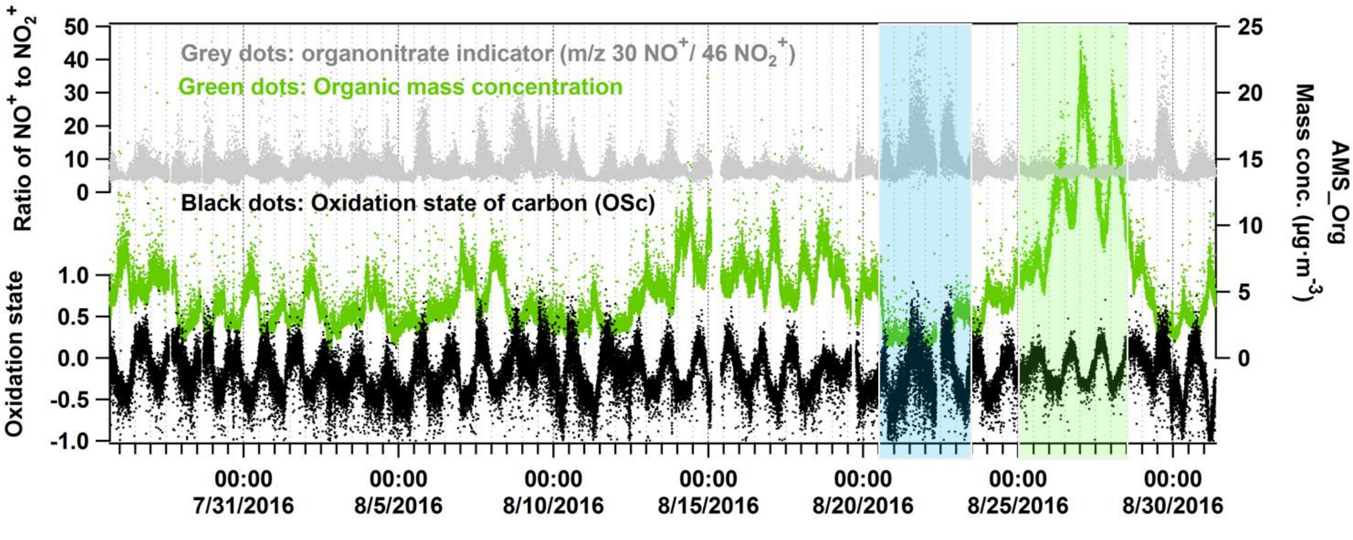

Figure S7: Time series of organonitrate fraction indicator (grey dots) and oxidation state (black dots). The first (blue) and second (green) shaded areas mark the sodium chloride rich and organic rich episodes, respectively.

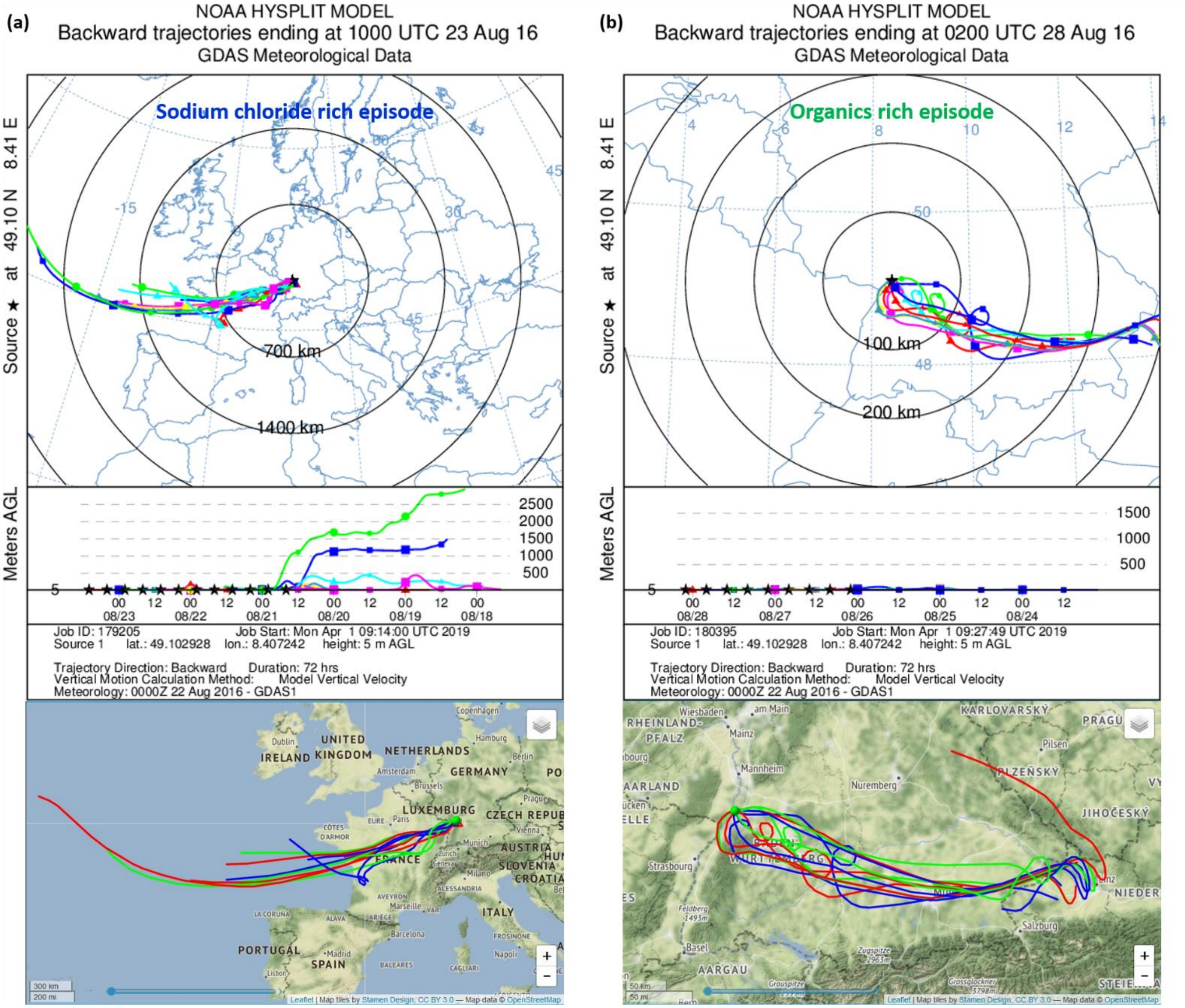

Figure S8: Hybrid Single-Particle Lagrangian Integrated Trajectory (HYSPLIT) back-trajectory analysis for 72 hours for sodium chloride rich (a) and organics rich (b) episodes, respectively.

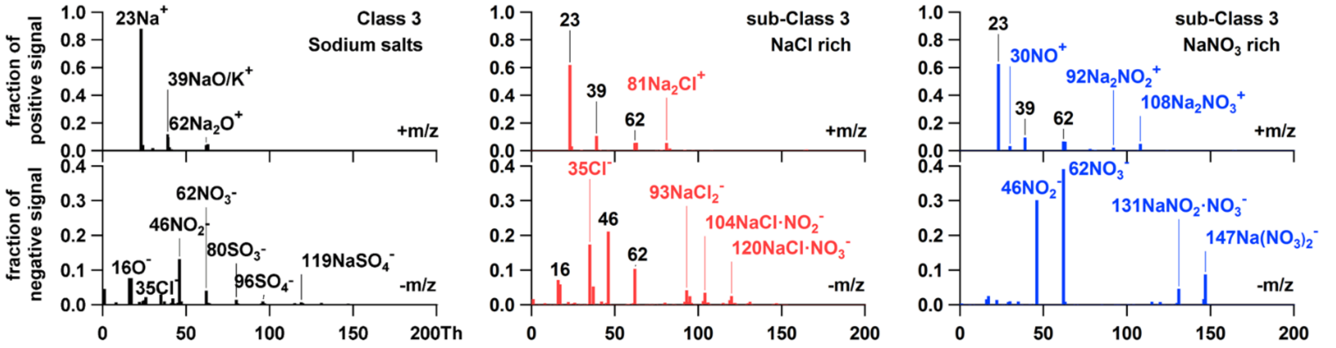

Figure S9: Spectra of the sodium salts class (Shen et al., 2019) and its sub-classes: NaCl rich (averaged from 1487 particles) and $NaNO_3$ rich (averaged from 300 particles).

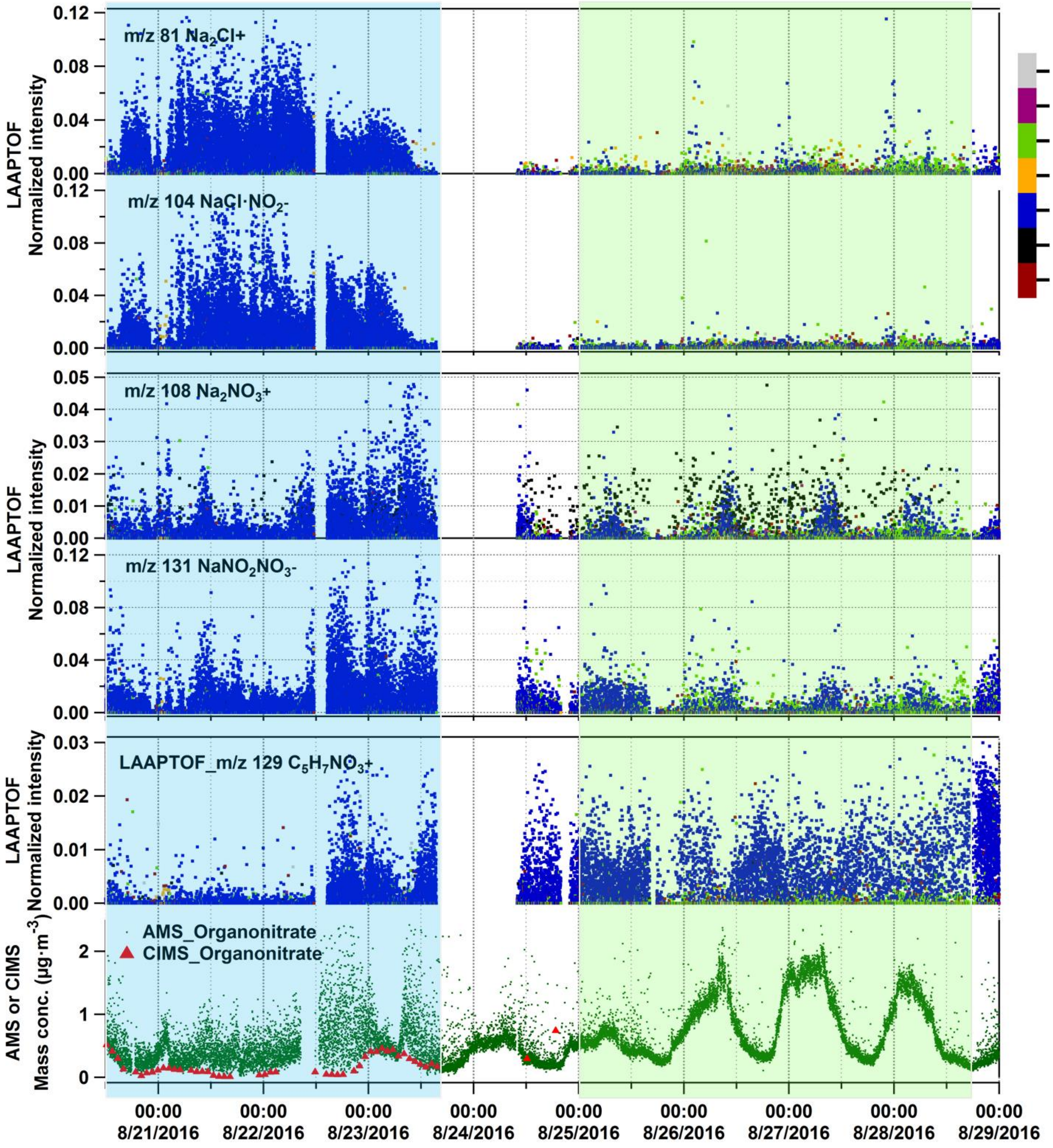

Figure S10: Time series of sodium chloride and nitrate, and organonitrate signatures in LAAPTOF mass spectra, as well as organonitrate mass concentration derived from AMS and FIGAERO-HR-ToF-CIMS (stands for a filter inlet for gases and aerosols coupled to a high-resolution time-of-flight chemical ionization mass spectrometer, hereafter CIMS) measurement. For LAAPTOF results, Y-axis is the normalized ion intensity (each ion peak intensity is normalized to the sum of all ion signals; positive and negative ions were analysed separately). The seven classes are class 1: calcium-Soil; class 2: aged soot; class3: sodium salts; class 4: secondary inorganics-amine; class 5: biomass burning-soil; class 6: biomass burning-organosulfate; and class 7: mixed/aged-dust. Obvious sodium chloride and nitrate signatures are mainly found in class 3 labelled in blue colour. AMS and CIMS results (Pearson's correlation coefficient γ=0.52) are adapted from our companion study by Huang et al (2019). It should be noted that during the sodium chloride rich episode (first band in blue) the fraction of organonitrates is higher (Fig. S7), although the organonitrate mass concentration is lower than that during the organic rich episode (second band in green).

The method to estimate organonitrates based on AMS measurement can be referred to Farmer et al. (2010) and the parameters used here are the same as that used by Huang et al. (2019). The result in Fig. S10 is based on our AMS measurements and the corresponding equation suggested by Farmer et al. (2010), as follows:

$$y=[(Robs-Ran)(1+Ron)]/[(Ron-Ran)(1+Robs)] \qquad (S1)$$

where y is the estimated fraction of organic nitrate in the total nitrate measured by the AMS, Robs is the observed ambient ratio of NO_2^+/NO^+; Ran and Ron are the NO_2^+/NO^+ ratio for ammonium nitrate and organonitrate, respectively. In our study Ran=0.43 based on the measurement and Ron=0.1 based on literature data. More details can be found by Huang et al. (2019).

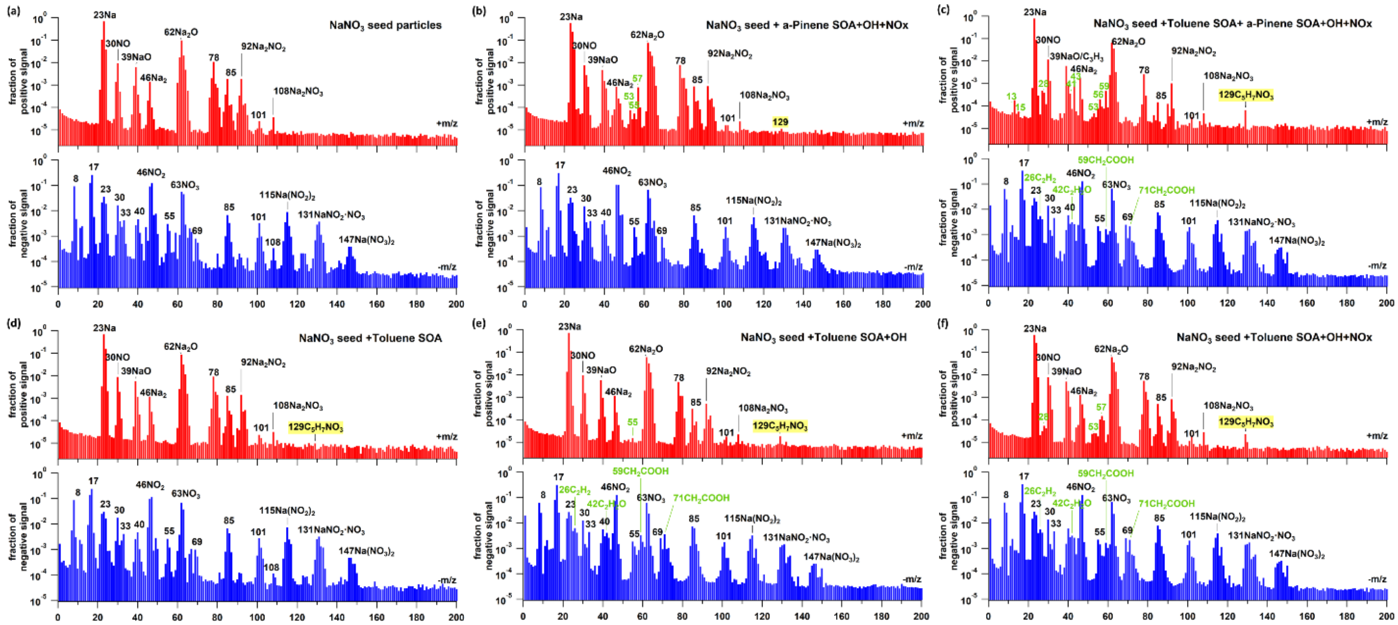

Figure S11: Laboratory evidence for anthropogenic organonitrate (LAAPTOF signature m/z 129 $C_5H_7NO_3^+$). (a) to (f) are the averaged spectra from several thousand single particles, respectively. Y-axis is the normalized ion intensity (each ion peak intensity is normalized to the sum of all ion signals; positive and negative ions were analysed separately).

Regarding organonitrate, we have found some laboratory evidence for its potential origin. AIDA (aerosol interaction and dynamics in the atmosphere) simulation chamber studies have been done with α-pinene and/or toluene OH oxidations on $NaNO_3$ seeds in the presence/absence of NO_x. The corresponding single particle spectra are shown in Fig. S11. It turns out that m/z 129+ is quite weak in α-pinene system even with NO_x (panel b), but it is much stronger after toluene is added (panel c). In the toluene system (refer to panel d to f), m/z 129+ is already present when $NaNO_3$ seeds are coated with toluene derived secondary organic aerosol (SOA) (panel d), likely due to the recombined fragments from toluene and nitrate. After adding extra OH, m/z 129+ is becoming stronger, likely due to the more aged toluene SOA (panel e). When NOx is added to toluene system, m/z 129+ becomes much stronger (panel f), likely due to the organonitrate formation. Hence, we can conclude that m/z 129 $C_5H_7NO_3^+$ is more related to toluene rather than α-pinene, namely m/z 129 $C_5H_7NO_3^+$ could be a signature peak for anthropogenic sources in LAAPTOF spectra.

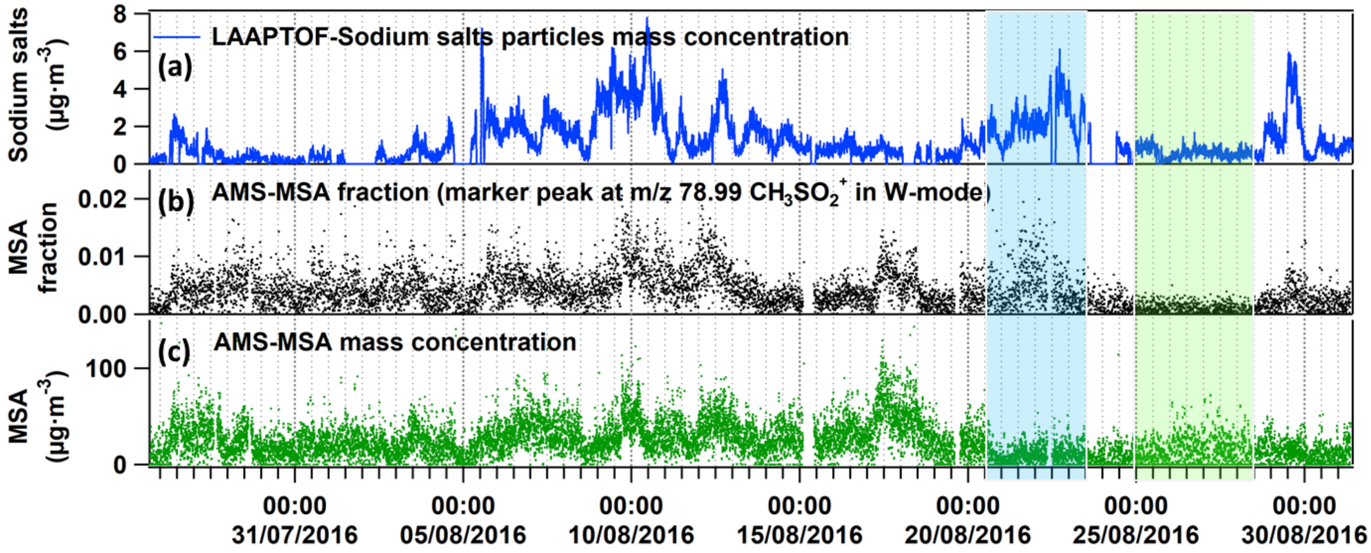

Figure S12: Time series of the estimated mass concentration of sodium salts particles measured by the LAAPTOF (a), methanesulfonic acid (MSA) fraction to total organics and sulfate measured by the AMS (b) and MSA mass concentration (c). The first (blue) and second (green) shaded areas mark the sodium chloride rich and organic rich episodes, respectively.

The method used to estimate MSA fraction (f_{MSA}, signal fraction of MSA to total org and sulfate) and its mass concentration can be referred to Huang et al. (2015). In brief, W-mode f_{MSA} is calculated and then used to multiply V-mode mass concentration of organics and sulfate, resulting estimated MSA mass concentration. The corresponding equations are as follows:

$$\sum \mathrm{I_{MSA}} = \frac{\mathrm{I_{CH3SO2}}}{9.7\%} \tag{S2}$$

$$\mathrm{f_{MSA}} = \frac{\frac{\sum \mathrm{I_{MSA}}}{\mathrm{RIE_{MSA}}}}{\frac{\sum \mathrm{I_{Org}}}{\mathrm{RIE_{Org}}} + \frac{\sum \mathrm{I_{SO4}}}{\mathrm{RIE_{SO4}}}} \tag{S3}$$

$$\mathrm{C_{MSA}} = \mathrm{f_{MSA}} \times (\mathrm{C_{Org}} + \mathrm{C_{SO4}}) \tag{S4}$$

where $\sum \mathrm{I_{MSA}}$ is the total signal intensity of all MSA fragments measured in W-mode, which can be estimated based on the fragmentation patterns determined from the laboratory experiments (Huang et al., 2015). It was reported that the signal intensity of marker peak at m/z 78.99 ($CH_3SO_2^+$) accounted for (9.7 ± 1.6) % of the total signal intensity of all MSA fragments. $\sum \mathrm{I_{Org}}$ and $\sum \mathrm{I_{SO4}}$ are total signal intensity of organics and sulfate fragments measured in W-mode, respectively. Relative ion efficiency of MSA ($\mathrm{RIE_{MSA}}$=1.3) is the averaged value from $\mathrm{RIE_{Org}}$ (=1.4) and $\mathrm{RIE_{SO4}}$ (=1.2). $\mathrm{C_{Org}}$ and $\mathrm{C_{SO4}}$ are mass concentrations calculated from V-mode data. $\mathrm{C_{MSA}}$ is the estimated MSA mass concentration.

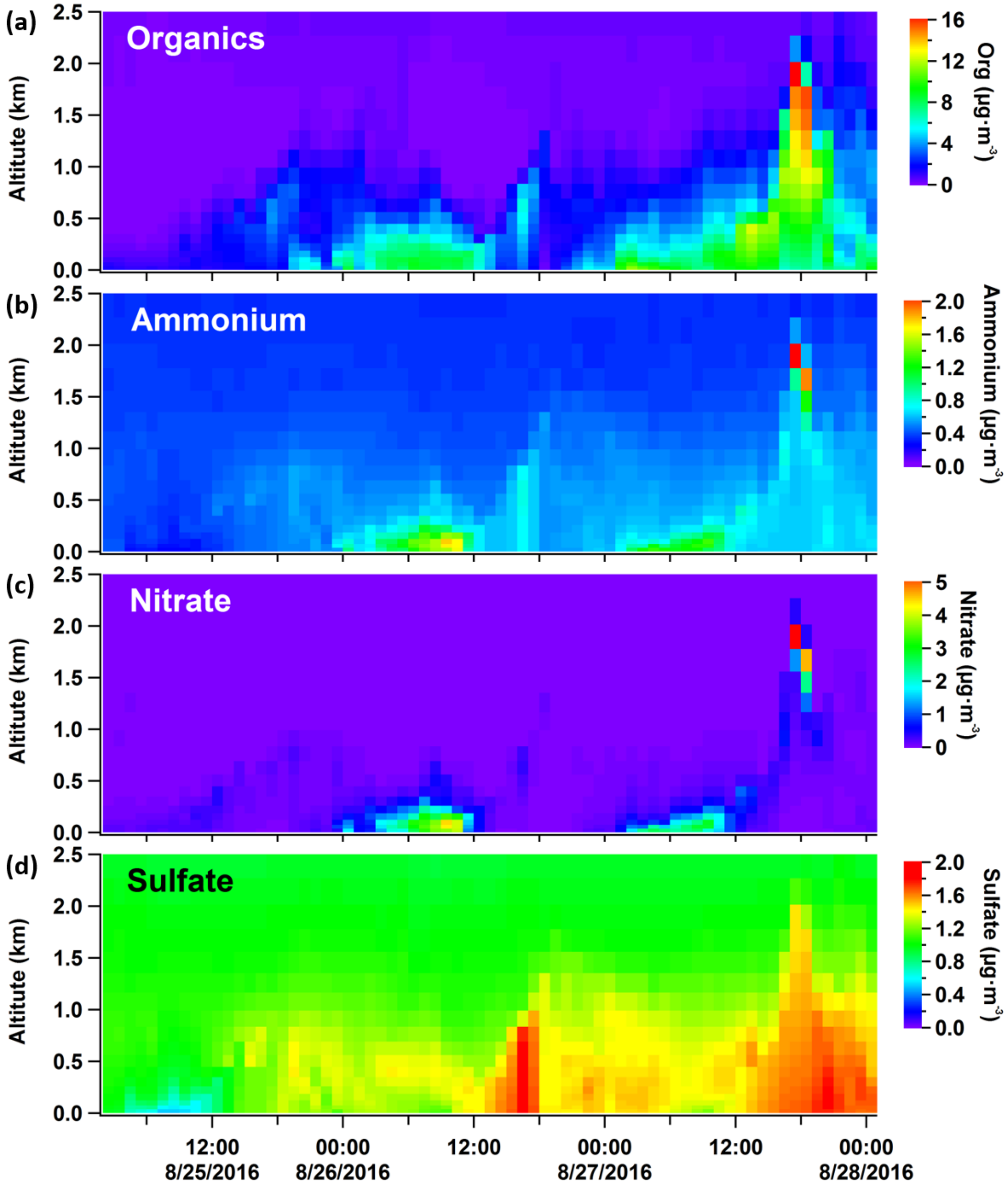

Figure S13: Time series of vertical profiles for organics, ammonium, nitrate, and sulfate as calculated by COSMO-ART.

References

Farmer, D. K., Matsunaga, A., Docherty, K. S., Surratt, J. D., Seinfeld, J. H., Ziemann, P. J., and Jimenez, J. L.: Response of an aerosol mass spectrometer to organonitrates and organosulfates and implications for atmospheric chemistry, P Natl Acad Sci USA, 107, 6670–6675, 2010.

Huang, D. D., Li, Y. J., Lee, B. P., and Chan, C. K.: Analysis of Organic Sulfur Compounds in Atmospheric Aerosols at the HKUST Supersite in Hong Kong Using HR-ToF-AMS, Environ Sci Technol, 49, 3672–3679, 2015.

Huang, W., Saathoff, H., Shen, X. L., Ramakrishna, R., Leisner, T., and Mohr, C.: Chemical characterization of highly functionalized organonitrates contributing to high night-time organic aerosol mass loadings and particle growth, Environ Sci Technol, 53, 1165–1174, 2019.

Zhang, Q., Jimenez, J. L., Canagaratna, M. R., Ulbrich, I. M., Ng, N. L., Worsnop, D. R., and Sun, Y. L.: Understanding atmospheric organic aerosols via factor analysis of aerosol mass spectrometry: a review, Anal Bioanal Chem, 401, 3045–3067, 2011.

Five supporting videos (.gif files) are available at KIT open data (https://doi.org/10.5445/IR/1000094401).

1. SI_PN_10m.gif

Particle number concentrations and wind field calculated by COSMO-ART during high SO_2 period (from 20160826 0:00 to 13:00 (local time) for 10 m a.g.l.

2. SI_PN_122m.gif

Particle number concentrations and wind field calculated by COSMO-ART during high SO_2 period from 20160826 0:00 to 13:00 (local time) for 122 m a.g.l.

3. SI_Org1_10m.gif

Particulate organic mass concentrations and wind field calculated by COSMO-ART from 20160825 17:00 to 20160826 18:00 (local time) for 10 m a.g.l.

4. SI_Org2_10m.gif

Particulate organic mass concentrations and wind field calculated by COSMO-ART from 20160826 18:00 to 20160827 12:00 (local time) for 10 m a.g.l.

5. SI_Org3_10m.gif

Particulate organic mass concentrations and wind field calculated by COSMO-ART from 20160827 12:00 to 20160828 01:00 (local time) for 10 m a.g.l.